Energy Conversion and Management 313 (2024) 118584

Contents lists available at ScienceDirect

Energy Conversion and Management

journal homepage: www.elsevier.com/locate/enconman

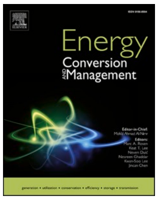

Research Paper

# Innovative design of an annular thermoelectric generator for enhanced automotive waste heat recovery

Ding Luo [a,b,*], Haokang Zhang [a], Jin Cao [a], Yuying Yan [c], Bingyang Cao [b,*]

[a] *Collaborative Innovation Center for Microgrid of New Energy, College of Electrical Engineering & New Energy, China Three Gorges University, Yichang, China*
[b] *Key Laboratory for Thermal Science and Power Engineering of Ministry of Education, Department of Engineering Mechanics, Tsinghua University, Beijing 100084, China*
[c] *Faculty of Engineering, University of Nottingham, University Park, Nottingham, UK*

ARTICLE INFO

*Keywords:*
Thermoelectric generator
Waste heat recovery
Thermoelectric module
Temperature drop
Numerical simulation

ABSTRACT

The annular thermoelectric generator (ATEG) gains significant attention in the automotive waste heat recovery field due to its compatibility with the exhaust pipe's shape. To address the performance deterioration issue due to the temperature drop, a novel annular thermoelectric module (ATEM) structure is proposed, in which the cross-sectional area of the thermoelectric elements continuously increases along the direction of heat flow. To assess the performance and perform parameter optimizations, this work develops a three-dimensional, steady-state, and fluid-thermal-electric multiphysics numerical model of the entire ATEG. The length difference of thermoelectric elements in different columns (ΔL) is comprehensively optimized through numerical simulations, and the effects of exhaust temperature and velocity on the optimal ΔL value are studied. The results indicate that a great temperature drop exists inside the ATEM, suggesting the advantages and effectiveness of the proposed novel structure configuration for modules. The optimal ΔL value is not sensitive to the exhaust gas temperature and velocity, and when ΔL = 0.06 mm, the novel ATEG achieves the highest output performance, with an output power of 76.66 W and an output efficiency of 1.45 % at the exhaust gas temperature of 550 K and the exhaust gas velocity of 30 m/s. The power and efficiency experience an improvement of 8.97 % and 8.93 %, respectively, compared to the traditional structure. Additionally, the lower exhaust gas temperature and velocity contribute to a greater performance improvement for the novel ATEG. This ATEM structural design provides a new approach to enhance performance when encountering temperature drop issues.

**Nomenclature.**

| | |
|---|---|
| *Symbols* | |
| $A$ | area, $m^2$ |
| $c$ | specific heat, $J\cdot kg^{-1}\cdot K^{-1}$ |
| $\overrightarrow{E}$ | electric field density vector, $V\cdot m^{-2}$ |
| $H$ | height, mm |
| $\overrightarrow{J}$ | current density vector, $A\cdot m^{-2}$ |
| $k$ | turbulent kinetic energy, $m^2\cdot s^{-2}$ |
| $L$ | length, mm |
| ΔL | the length difference, mm |
| $\dot{m}$ | mass flow rate, $g\cdot s^{-1}$ |
| n | number |
| $p$ | pressure, Pa |
| $P$ | output power, W |
| $Q$ | heat absorption, W |
| $r$ | inner radius |
| $R$ | electric resistance, Ω |
| $\dot{S}$ | source term |
| $T$ | temperature, K |
| $U$ | output voltage, V |
| $\overrightarrow{v}$ | velocity, $m\cdot s^{-1}$ |
| *Abbreviations* | |
| ATEG | annular thermoelectric generator |
| ATEM | annular thermoelectric module |
| *Subscripts* | |
| a | ambient |
| co | copper sheets |
| ex | exhaust |
| in | exhaust inlet surface |
| out | exhaust outlet surface |
| i | ith, i = 1, 2, 3, …… |
| j | jth, j = 1, 2, 3, …… |

(*continued on next page*)

---

* Corresponding authors.
*E-mail addresses:* Ding_L@outlook.com (D. Luo), caoby@tsinghua.edu.cn (B. Cao).

https://doi.org/10.1016/j.enconman.2024.118584
Received 28 February 2024; Received in revised form 26 April 2024; Accepted 19 May 2024
Available online 29 May 2024

(*continued*)

| | |
|---|---|
| L | load resistance |
| m | material |
| N | n-type thermoelectric elements |
| P | p-type thermoelectric elements |
| t | vehicle transmission system |
| *Greek symbols* | |
| $\alpha$ | Seebeck coefficient, $\mu V\cdot K^{-1}$ |
| $\sigma^{-1}$ | electrical resistivity, $\Omega\cdot m$ |
| $\phi$ | electrical potential, V |
| Î¸ | angle |
| $\eta$ | efficiency |
| $\rho$ | density, $kg\cdot m^{-3}$ |
| $\lambda$ | thermal conductivity, $W\cdot m^{-1}\cdot K^{-1}$ |
| $\mu$ | dynamic viscosity, $Pa\cdot s$ |
| $\varepsilon$ | turbulent dissipation rate, $m^2\cdot s^{-3}$ |

## 1. Introduction

Fuel-powered vehicles exhibit an energy utilization rate of only 30 %, with around 40 % of the total energy generated from fuel combustion dissipating as heat through the vehicle's exhaust system [1,2]. Recovering the wasted heat in the vehicle exhaust can improve the energy utilization rate, and researchers have proposed various heat recovery technologies, such as thermoelectric power generation [3–5], organic Rankine cycle [6,7], thermophotovoltaic [8], and Kalina cycle-based systems [9,10]. Among these technologies, thermoelectric generators, featuring unique advantages such as simple structure, light weight, high reliability, and long lifespan, demonstrate broad prospects for development in automobile exhaust heat recovery.

Currently, the thermoelectric output efficiency of thermoelectric generators employed for recovering exhaust heat falls below the threshold required for commercial applications. Researchers mainly focus on improving the thermoelectric output efficiency of thermoelectric generators by developing high ZT values thermoelectric materials or optimizing their structures. Nowadays, with the development of nanotechnology and quantum-scale synthesis technology, the ZT values of some thermoelectric materials have approached the threshold of commercial application [11,12]. However, the high ZT values reported in the literature are often achieved through the micro regulation of material structure, which cannot be stably synthesized, and their costs cannot meet the requirements of mass production. Therefore, the structural optimization method for thermoelectric generators is an alternative promising solution to boost the thermoelectric output efficiency, which can be classified into two aspects: one is to optimize the structure of the heat exchanger, and the other is to optimize the structure of the thermoelectric module.

For the structural optimization of heat exchangers: Luo et al. [13] proposed a convergent thermoelectric generator employing a convergent heat exchanger at a suitable inclination angle. This innovative design notably enhances both the hot end temperature and the net output power of the thermoelectric generator. Zhu et al. [14] introduced a new twisted belt annular thermoelectric generator (ATEG), integrating a tie within the heat exchanger to enhance heat transfer between the exchanger and exhaust gas. Yang et al. [15] presented a concentric ATEG composed of the annular thermoelectric module (ATEM) and concentric annular heat exchanger; Thanks to a substantial enhancement in the total heat transfer coefficient, the proposed ATEG experienced a maximum net power increase of 65 % compared with the traditional structure. Chen et al. [16] improved heat transfer efficiency in the heat exchanger by employing a fin structure; Although the pressure drop was increased with the use of fins in the exhaust channel, the backpressure power loss only accounted for less than 1 % of the total output power at low Reynolds numbers ($Re = 10–1000$), indicating that incorporating fins can notably improve in both heat transfer and thermoelectric generator performance. M. Eldin et al. [17] proposed a new type of finned needle porous heat exchanger, where the output power of the recovery system was increased by 45 % – 110 % compared to the traditional ATEG with a smooth channel. Li et al. [18] introduced porous foam copper to the central flow area of the heat exchanger to augment its heat transfer performance, where the output power of the thermoelectric generator increases by a factor of 2.3 when compared to an insert-free thermoelectric generator. Yang et al. [19] proposed a scheme using a silicone polymer-based thermal conductive oil for the transfer of exhaust heat and designed an innovative concentric tube heat exchanger; Their results indicated that compared to the traditional ATEG, the maximum output power of the new ATEG is increased by 15.2 %. However, modifications in the heat exchanger structure often introduce an increased pressure drop, leading to backpressure power loss, and could potentially bring about a decrease in the overall energy utilization rate of the system [20]. The ATEG stands out as an excellent option for thermoelectric waste heat recovery, thanks to the smooth flow from the exhaust pipe to the annular heat exchanger, resulting in extremely low backpressure loss.

For the structural optimization of thermoelectric modules: the traditional thermoelectric module design consists of a planar π-shaped configuration, with p-type and n-type thermoelectric elements of equal size and composed of a single thermoelectric material. To significantly enhance the thermoelectric performance, researchers have suggested several advanced thermoelectric module structures. Wang et al. [21] proposed an X-type thermoelectric module and optimized its tilt angle through numerical simulation; Their findings revealed that a tilt angle of 10° enables the maximum output power, achieving a 4.57 % increase compared to the conventional structure. Shen et al. [22] presented a segmented ATEM consisting of two thermoelectric materials with different optimal working temperatures and analyzed its performance using a theoretical model; Their research shows that the performance of ATEG has significantly improved attributable to the utilization of the segmented ATEM. Similar to segmented thermoelectric modules, researchers [23] have proposed a structural design of two-stage modules, where two thermoelectric modules are stacked together and the heat flows through the first and second thermoelectric modules in sequence. This design is well-suited for use in applications featuring large temperature differences. Soheil Asaadi et al. [24] conducted three-dimensional simulations on a two-stage ATEM, revealing a significantly superior output performance compared to a single-stage ATEM. In the application of waste heat recovery, the flat design of thermoelectric modules has been widely studied. However, in engineering applications such as automotive exhaust waste heat recovery [25], wearable devices [26], and industrial waste heat recovery [27], the heat source surface is not smooth, but usually presents a curved structure, in which case the direct installation of flat thermoelectric modules will cause additional contact thermal resistance and thermal losses [28,29], resulting in the inefficient utilization of heat. On the contrary, ATEMs may be more suitable for integration with tube heat exchangers and mass production. Huang et al. [30] proposed an ATEM that matches the geometry of an automobile exhaust pipe and compared its performance with traditional flat thermoelectric modules, the research findings demonstrated that the ATEM outperforms the flat thermoelectric module, with an average net power increase of 1.1 %. In addition, the ATEM has also shown its application prospects in fields such as flexible micro-light-emitting diodes [31], annular solar thermoelectric generators [32], and cold energy recovery of liquefied natural gas [33].

The above-mentioned advanced structures have greatly improved the performance of thermoelectric generators. However, in the utilization of thermoelectric generators for automotive exhaust heat recovery, a downward flow of exhaust gas causes its heat to be absorbed by the exhaust pipe, resulting in a decline in the hot end temperature and generated current of thermoelectric elements along the downward direction. The output current of the complete thermoelectric module is constrained by the serial arrangement of thermoelectric elements, determined by the minimum current of the individual element, thereby leading to electrical power losses. In response to this issue, Lu et al. [34]

adopted an unevenly distributed fin structure in the heat exchanger to improve the temperature uniformity of the hot side surface, effectively enhancing the output performance of TEG. Furthermore, optimizing the structure of TEMs is a more direct solution. Previous studies [35,36] have reported that adjusting the cross-sectional area of each thermoelectric element according to its temperature difference is an effective strategy for addressing the problem of limited current; This method ensures that all thermoelectric elements generate the same current, allowing for maximum conversion of absorbed heat energy into electrical energy.

Based on the concept of equalizing the output current of all thermoelectric elements through dimension regulation, a novel ATEG for waste heat recovery from automotive exhaust is proposed in this work, where the cross-sectional area of the thermoelectric element increases continuously along the direction of exhaust flow. Besides, the geometric tolerances between different columns of thermoelectric elements in the ATEM are optimized to maximize the output performance of the ATEG. To evaluate the performance and guide the structural parameter optimization of the proposed ATEG, a three-dimensional, steady-state, and thermal-electric-fluid model is established. The outcomes of this research may provide crucial guidance for the optimization, theoretical analysis, and structural design of the ATEG.

## 2. Structure of the novel ATEG

When applied to the waste heat recovery from automotive exhaust, the ATEG features the advantages of extremely low backpressure loss and easy-to-system integration. The proposed ATEG consists of an annular finned heat exchanger for absorbing exhaust heat, five ATEMs for power generation, and a radiator for heat dissipation. Here, a water-cooled radiator is applied. Owing to the considerable specific heat capacity and high cooling performance of water cooling, the cold end temperature of the ATEM is almost the same [35,37]. Therefore, the radiator of the ATEG is simplified during numerical simulations and replaced as a constant temperature boundary condition at the cold end of the ATEM. The structural diagram of the novel ATEG is shown in Fig. 1(a), with 5 novel ATEMs uniformly arranged on the surface of the heat exchanger. The annular heat exchanger (with an overall length of 200 mm) is composed of 2 concentric tube walls and 40 uniformly distributed fins, with the purpose of enhancing the heat transfer from the exhaust gas to the heat exchanger. The length of the fins is the same as that of the heat exchanger, which is 200 mm. The automotive exhaust flows through the gaps between the fins, and the center angle of the gaps is the same as that of the fins, both at 4.5°. Besides, the height of the fins is 15 mm. The outer wall diameter of the annular heat exchanger is 50 mm, which can match the diameter of automotive exhaust pipes. Fig. 1 (b) and Table 1 give the detailed radius of different components of the ATEG.

The ATEM consists of substrates, copper conductive sheets, and P-type and N-type thermoelectric elements, all presenting an annular structure, as shown in Fig. 2. Among them, P-type thermoelectric elements and N-type thermoelectric elements are connected in series through copper conductive sheets and sandwiched between two concentric ring-shaped substrates. Five ATEMs are consistent and connected in series through two terminal copper electrodes of each ATEM, as marked in A and B in Fig. 2. The ATEM contains *n* rows of annular thermoelectric elements. In the traditional ATEM, all P-type and N-type thermoelectric elements feature identical geometric parameters. However, when using the traditional ATEM to recover automotive exhaust heat, the substantial temperature decrease along the downward flow of exhaust gas will lead to an electrical power loss.

To address this defect, a novel ATEM structure is proposed, in which the cross-sectional area of the thermoelectric elements continuously increases with the direction of heat flow. Here, the ATEM is divided into *n* rows of thermoelectric elements, with the first row being close to the inlet direction of the heat flow, and the *n*th row being close to the outlet direction. $\theta_{P/N}$ and Î¸$_{1}$ represent the center angle of the P/N type thermoelectric elements and the center angle of the distance between them, which are 6° and 3°, respectively. The height of the substrate, copper

**Table 1**
Structural parameters of the novel ATEG.

| Parameter | Description | Value | Unit |
|---|---|---|---|
| $r_1$ | Radius of heat exchanger inner wall | 9.2 | mm |
| $r_2$ | Radius of fins | 10 | mm |
| $r_3$ | Radius of heat exchanger outer wall | 25 | mm |
| $r_4$ | Radius of lower annular substrates | 26 | mm |
| $r_5$ | Radius of lower annular copper connectors | 26.8 | mm |
| $r_6$ | Radius of thermoelectric elements | 27.1 | mm |
| $r_7$ | Radius of upper annular copper connectors | 29.1 | mm |
| $r_8$ | Radius of upper annular substrates | 29.4 | mm |

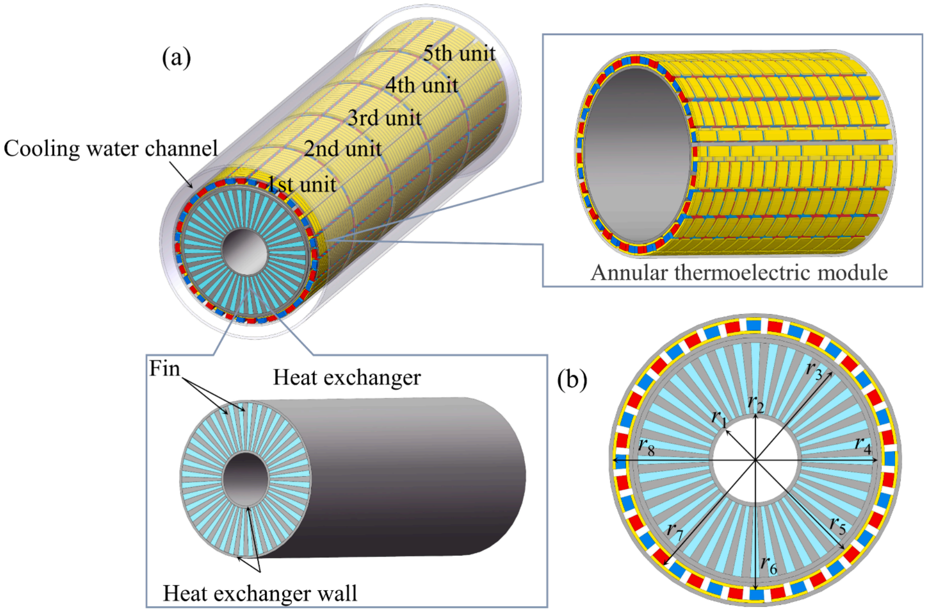

**Fig. 1.** Schematic diagram of the novel ATEG. (a) 3D Architecture diagram; (b) 2D View of structural parameters.

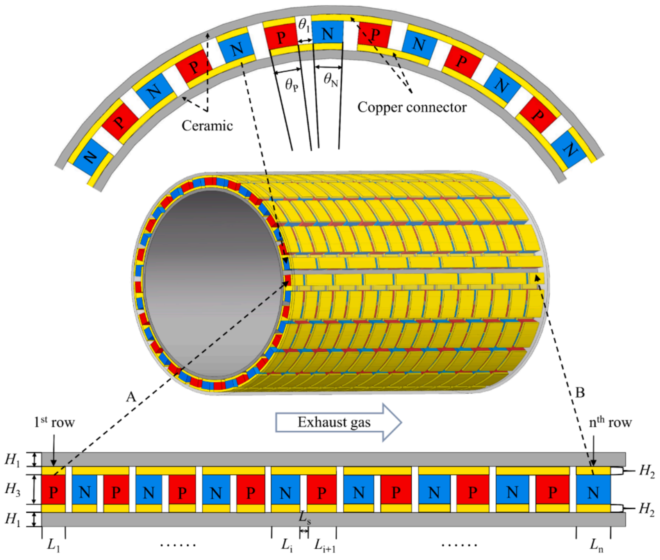

**Fig. 2.** Schematic of the novel ATEM.

conductive sheet, and thermoelectric element is H1 = 0.8 mm, H2 = 0.6 mm, and H3 = 2 mm, respectively. Unlike the traditional structure, the difference of the proposed ATEM is that the length of the ith column thermoelectric element ($L_i$) differs from the length of the i + 1th column thermoelectric element (Li + 1), where $i = 1, 2, \ldots, n$. The relationship between $L_i$ and Li + 1 is given by $\Delta L = L_{i+1} - L_i$, to ensure that the cross-sectional area of the thermoelectric element gradually increases along the direction of heat flow. To maximize the output performance of the ATEG, the value of ΔL is optimized within a specific range (0, 0.02 mm, 0.04 mm, 0.06 mm, 0.08 mm) in the following section. When ΔL = 0, the ATEM presents a traditional structure, while when ΔL = (0.02 mm, 0.04 mm, 0.06 mm, 0.08 mm), the cross-sectional area of thermoelectric elements increases continuously along the heat flow direction. The ATEMs with different ΔL values keep the same overall area of thermoelectric elements, to avoid the performance improvement of the novel ATEM being caused by an increase in the use of thermoelectric materials. For this goal, the cross-sectional area of the first row of thermoelectric elements in ATEMs with lower ΔL values is greater than that of the first row of thermoelectric elements in ATEMs with higher ΔL values. Table 2 provides a thorough overview of the material parameters for the ATEG, including specific references to thermoelectric material parameters derived from Ref. [38].

## 3. Numerical model

To investigate the optimal ΔL value and estimate the ATEG performance, a comprehensive fluid-thermal-electric multiphysics numerical model is built on the COMSOL commercial software platform. The model simulation is based on the following assumptions: (i) Neglecting gravity and thermal radiation; (ii) Thermoelectric materials are isotropic; (iii) Air properties are used as those of exhaust gas, and temperature dependence of air is considered.

### 3.1. Governing equations

The governing equations for the multiphysics numerical model of the ATEG encompass transport equations within distinct calculation domains. In the fluid region of automotive exhaust, the steady-state equations for the conservation of mass, momentum, and energy are articulated as follows:

$$\nabla\cdot\overrightarrow{v} = 0 \tag{1}$$

$$\nabla\cdot(\overrightarrow{v}\,\overrightarrow{v}) = -\frac{1}{\rho}\nabla p + \nabla\cdot(\mu\nabla\overrightarrow{v}) \tag{2}$$

$$\nabla\cdot(\lambda\nabla T) = \rho c\overrightarrow{v}\cdot\nabla T \tag{3}$$

Also, the simulation of fluid flow in the exhaust gas employs the standard k − ε turbulence model, as described in Ref. [39]. This turbulence model can be expressed as follows:

$$\rho(\overrightarrow{v}\cdot\nabla)k = \nabla\cdot\left[\left(\mu+\frac{\mu_t}{\sigma_k}\right)\nabla k\right] + G_K - \rho\varepsilon \tag{4}$$

$$\rho(\overrightarrow{v}\cdot\nabla)\varepsilon = \nabla\cdot\left[\left(\mu+\frac{\mu_t}{\sigma_\varepsilon}\right)\nabla \varepsilon\right] + C_{1\varepsilon}\frac{\varepsilon}{k}G_k - C_{2\varepsilon}\rho\frac{\varepsilon^2}{k} \tag{5}$$

$$\mu t = \rho C_\mu\frac{k^2}{\varepsilon} \tag{6}$$

where $C_{1\hat{\text{I}}\mu}$, $C_{2\hat{\text{I}}\mu}$, $C_\mu$, $\sigma_k$, and $\sigma_\varepsilon$ are empirical constants.

Within the solid regions encompassing heat transfer, including substrates and the annular finned heat exchanger, the steady-state energy conservation equation is expressed as follows:

**Table 2**
Material properties of the novel ATEG.

| Name | Material | Property | Value | Unit |
|---|---|---|---|---|
| Heat exchanger | Aluminum | Thermal conductivity | 238 | W/(m·K) |
| Substrate | Alumina | Thermal conductivity | 35 | W/(m·K) |
| Conductive plate | Copper | Thermal conductivity | 398 | W/(m·K) |
| | | Electrical resistivity | 1.72 × 10-3 | 10-5ΩÂ·m |
| P-type thermoelectric element | $Bi_{0.44}Sb_{1.56}Te_3$ | Thermal conductivity | $1.8022 \times 10^{-10}T^4-2.8631 \times 10^{-7}T^3 + 1.7941 \times 10^{-4}T^2-0.052T + 6.8208$ | W/(mÂ·K) |
| | | Electrical resistivity | $-6.839 \times 10^{-10}T^4 + 9.9566 \times 10^{-7}T^3-5.3215\times10^{-4}T^2 + 0.1298T-11.506$ | 10-5ΩÂ·m |
| | | Seebeck coefficient | $1.9359 \times 10^{-8}T^4-3.7183 \times 10^{-5}T^3 + 2.4243 \times 10^{-2}T^2-6.366T + 772.02$ | μVÂ·K$^{-1}$ |
| N-type thermoelectric element | $Bi_2Te_{2.7}Se_{0.3}$ | Thermal conductivity | $-1.0263 \times 10^{-9}T^4 + 1.6523 \times 10^{-6}T^3-9.6842\times10^{-4}T^2 + 0.2447T-21.5585$ | W/(mÂ·K) |
| | | Electrical resistivity | $4.3486 \times 10^{-10}T^4-8.9267 \times 10^{-7}T^3 + 6.4322 \times 10^{-4}T^2-0.192T + 21.419$ | 10-5ΩÂ·m |
| | | Seebeck coefficient | $1.1468 \times 10^{-8}T^4-1.2129 \times 10^{-5}T^3 + 3.5018 \times 10^{-3}T^2-0.1535T-189.21$ | Î¼VÂ·K$^{-1}$ |
| Exhaust gas | Air | Specific heat | $1.2859 \times 10^{-13}T-6.0241 \times 10^{-10}T^3 + 9.4530 \times 10^{-7}T^2-3.7259 \times 10^{-4}T + 1.0476$ | kJ/(kgÂ·K) |
| | | Dynamic viscosity | $-1.0659 \times 10^{-10}T^4 + 4.6437 \times 10^{-7}T^3-7.6943 \times 10^{-4}T^2 + 0.8357T-8.3828$ | $10^{-7}$PaÂ·s |
| | | Thermal conductivity | $-7.4386 \times 10^{-15}T^4 + 4.1170 \times 10^{-11}T^3-7.9025 \times 10^{-8}T^2 + 1.1548 \times 10^{-4}T-2.2758 \times 10^{-3}$ | W/(mÂ·K) |

$$\nabla\cdot(\lambda\nabla T) = 0 \tag{7}$$

Within the solid regions that encompass both heat transfer and heat generation, including the copper electrodes and thermoelectric elements, the steady-state energy conservation equation is:

$$\nabla\cdot(\lambda m\nabla T) + \dot{S}_{\mathrm{m}} = 0 \tag{8}$$

where, subscript m designates distinct materials, $\dot{\mathrm{S}}_{\mathrm{m}}$ signifies the energy source term. In different material regions, $\dot{\mathrm{S}}_{\mathrm{m}}$ can be expressed as [40]:

$$\dot{S}_{\mathrm{m}} = \begin{cases} \sigma_{\mathrm{P}}^{-1}(T)\vec{J}^{2} - T_{\mathrm{P}}\nabla\alpha_{\mathrm{P}}(T)\vec{J} - \dfrac{\partial\alpha_{\mathrm{P}}(T)}{\partial T_{\mathrm{P}}}T_{\mathrm{P}}\vec{J}\cdot\nabla T; \text{P - type thermoelectric element} \\ \sigma_{\mathrm{N}}^{-1}(T)\vec{J}^{2} - T_{\mathrm{N}}\nabla\alpha_{\mathrm{N}}(T)\vec{J} - \dfrac{\partial\alpha_{\mathrm{N}}(T)}{\partial T_{\mathrm{N}}}T_{\mathrm{N}}\vec{J}\cdot\nabla T; \text{N - type thermoelectric element} \\ \sigma_{\mathrm{co}}^{-1}\vec{J}^{2}; \text{copper} \end{cases} \tag{9}$$

where the first term on the right-hand side of Eq. (9) signifies Joule heat, with the latter two terms denoting Peltier heat on junctions and Thomson heat along thermoelectric materials, respectively.

In solid regions where electrical current flow is present, the electric field transport equations are expressed as follows [41]:

$$\vec{E} = -\nabla\phi + \alpha_{\mathrm{P,N}}\nabla T \tag{10}$$

$$\vec{J} = \sigma_{\mathrm{m}}\vec{E} \tag{11}$$

$$\nabla\vec{J} = 0 \tag{12}$$

The foundational equations for governing the fluid-thermal-electric multiphysics numerical model are comprised of Eqs (1)-(12). Within this study, as the automobile exhaust flows through the heat exchanger, a significant reduction in temperature is evident, and the parameters of the thermoelectric material show a high correlation with temperature. Therefore, the temperature dependence of automotive exhaust and thermoelectric materials is considered. Additionally, variables, including temperature, mutually influence one another within the domains of the thermal field, electrical field, and flow field. Therefore, in this work, we concurrently solve the thermal field, electric field, and flow field to ensure precise calculations. A finite element method is employed for computing these equations in this work.

### 3.2. Boundary conditions

For the flow channel of exhaust gas, boundary conditions of velocity inlet and constant temperature are defined on the inlet surface, and the pressure boundary condition is defined on the outlet surface. Here, the ATEG is used to harvest exhaust heat from a passenger vehicle with a 3 L and 102 kW gasoline engine. According to the published data in Ref. [42], the produced exhaust mass flow rate and exhaust temperature are about 30 g/s (30 m/s for the given ATEG) and 550 K respectively. Therefore, the ranges of (15 m/s, 20 m/s, 25 m/s, and 30 m/s) and (400 K, 450 K, 500 K, and 550 K) are selected to study the influence of exhaust heat on the optimal configuration of the ATEM. For the cold side of the ATEM, a constant temperature of 300 K is defined on the cold-side surface of the ATEM, due to the use of water cooling [35]. In addition, the heat loss between the ATEM and the surroundings is considered, with the defining of convective heat transfer boundary on the surface of the solid region in contact with the external environmental gas, namely:

$$\lambda\frac{\partial T}{\partial n} = h_{\alpha}(T - T_{\alpha}) \tag{13}$$

where $h_{\mathrm{a}} = 10\ \mathrm{W\cdot m^{-2}\cdot K^{-1}}$ is the ambient convective heat transfer coefficient, and $T_{\mathrm{a}} = 293.15$ K is the ambient temperature.

In addition to the boundary conditions of the exhaust channel, ATEMs also need to apply reasonable boundary conditions for conducting numerical simulations. The terminals A and B (as shown in Fig. 2) of each ATEM are set as a grounded boundary and a circuit terminal respectively. To evaluate the output performance of the ATEM, a virtual additional circuit is introduced in the finite element model. The additional circuit contains a load resistor, with one end grounded and the other end connected to terminal B. Through a preliminary load analysis, it is found that the traditional ATEM reaches its highest output power when the load resistance value is 3.5 Ω. Considering the same internal resistance of ATEMs with different $\Delta L$ values due to the same overall cross-sectional area of thermoelectric elements, the load resistance is set to 3.5 Ω herein, to ensure the highest output performance. The detailed boundary parameters are shown in Table 3.

### 3.3. Parameter definition

By conducting finite element simulations, we can acquire information about the physical field distribution characteristics of the ATEG. Parameters such as voltage and temperature can be derived from the numerical results of specific cross-sectional analyses. The output power of an ATEM is calculated using the following formula:

$$P_{\mathrm{ATEM}} = \frac{U_{\mathrm{L}}^{2}}{R_{\mathrm{L}}} \tag{14}$$

Among them, $U_{\mathrm{L}}$ is the output voltage of the ATEM, and $R_{\mathrm{L}}$ is the load resistance. The overall output power of the ATEG is viewed as the sum of 5 ATEMs, which is:

$$P = \sum_{i=1}^{n=5} P_{\mathrm{ATEM}} \tag{15}$$

When the exhaust gas flows through the ATEG, the heat of the exhaust gas is absorbed through the manner of convective heat transfer, and the absorbed heat $Q_{\mathrm{h}}$ can be estimated by:

**Table 3**
Boundary conditions of the fluid-thermal-electric multiphysics numerical model for the ATEG.

| Control domain | Boundry | Value | Unit |
|---|---|---|---|
| ambient | temperature | 293.15 | K |
| exhaust gas | temperature inlet | 400,450,500,550 | K |
| | velocity inlet | 15,20,25,30 | m/s |
| | pressure outlet | 101.325 | kPa |
| cold side surface of ATEM | temperature | 300 | K |
| the A surface of the ATEM | circuit terminals | NA | NA |
| the B surface of the ATEM | grounding | 0 | V |
| surface in contact with the environment | ambient convection heat transfer coefficient | 10 | W/(m$^2$Â·K) |

$$Q_{\mathrm{h}} = c_{\mathrm{ex}}\dot{m}_{\mathrm{ex}}(T_{\mathrm{in}} - T_{\mathrm{out}}) \tag{16}$$

Among them, $T_{\mathrm{in}}$ and $T_{\mathrm{out}}$ are the temperatures of the exhaust gas inlet and outlet, respectively. $c_{\mathrm{ex}}$ is the specific heat of exhaust gas. $\dot{m}_{\mathrm{ex}}$ is the mass flow rate of exhaust gas, which can be estimated by:

$$\dot{m}_{\mathrm{ex}} = \rho v_{\mathrm{in}} A \tag{17}$$

with $v_{\mathrm{in}}$ and $A$ being the exhaust inlet velocity and cross-sectional area of the exhaust channel respectively.

Finally, the output efficiency of the ATEG can be expressed as:

$$\eta_{\mathrm{ATEG}} = \frac{P}{Q_{\mathrm{h}}} \tag{18}$$

### 3.4. Cell independence validation

Fig. 3 illustrates the finite element model of the ATEG. All cell structures are constructed using free tetrahedral cells, and boundary layers are defined at the interface between the exhaust gas and the heat exchanger. In light of the observed sensitivity of numerical simulation results to the cell parameters of the ATEG, four distinct cell systems, designated as Cell I, Cell II, Cell III, and Cell IV, have been employed to check cell independence. Here, boundary conditions of $T_{\mathrm{in}} = 550$ K and $v_{\mathrm{in}} = 30$ m/s are used for conducting simulations. Then, the output power of the ATEG is obtained and used to estimate the errors under different cell systems, as shown in Table 4. Augmenting the number of cells results in improved accuracy in numerical simulation results, but it also results in longer simulation times. To ensure high simulation accuracy and low computational cost simultaneously, Cell II is selected in this study.

### 3.5. Model validation

To validate the precision of the previously mentioned numerical model, the 3-D geometrical model of the TEG used in Ref. [36] is built, and its performance is simulated using the developed model. Fig. 4 illustrates the comparison of output performance between simulations in the present study and experiments in Ref. [36]. The maximum deviation of output power is lower than 6 %, affirming the high accuracy of the numerical model employed in this work for predicting the performance of the ATEG, and it can be used to steer performance analysis and structural parameter optimizations.

**Table 4**
Output power and error of the ATEG under different cell systems.

| Cell system | Cell number | Output power | Error | Simulation time |
|---|---|---|---|---|
| Cell I | 6,112,831 | 70.311 W | NA | 39.54 h |
| Cell II | 3,765,621 | 70.395 W | 0.12 % | 20.47 h |
| Cell III | 2,403,240 | 70.543 W | 0.33 % | 14.27 h |
| Cell IV | 1,677,837 | 70.712 W | 0.57 % | 11.62 h |

## 4. Results and discussion

In Sections 4.1 and 4.2, numerical simulations of the ATEG are conducted under boundary conditions of $v_{\mathrm{in}} = 30$ m/s and $T_{\mathrm{in}} = 550$ K, in order to highlight the effectiveness of the numerical model and explore the optimal value of ΔL, respectively. In Sections 4.3 and 4.4, the effect of exhaust temperature and velocity on the performance of the ATEG under different ΔL values is thoroughly investigated, respectively.

### 4.1. Numerical results and discussion

In this section, the ATEG with a value of ΔL = 0.06 mm is adopted to elucidate its distribution characteristics of different variables. Fig. 5 depicts the temperature distributions of the ATEM. Obviously, owing to the low thermal conductivity of thermoelectric elements, a substantial temperature gradient occurs from the hot side to the cold side of the ATEM, which is approximately 160 K. This temperature gradient drives the directional motion of charge carriers within thermoelectric

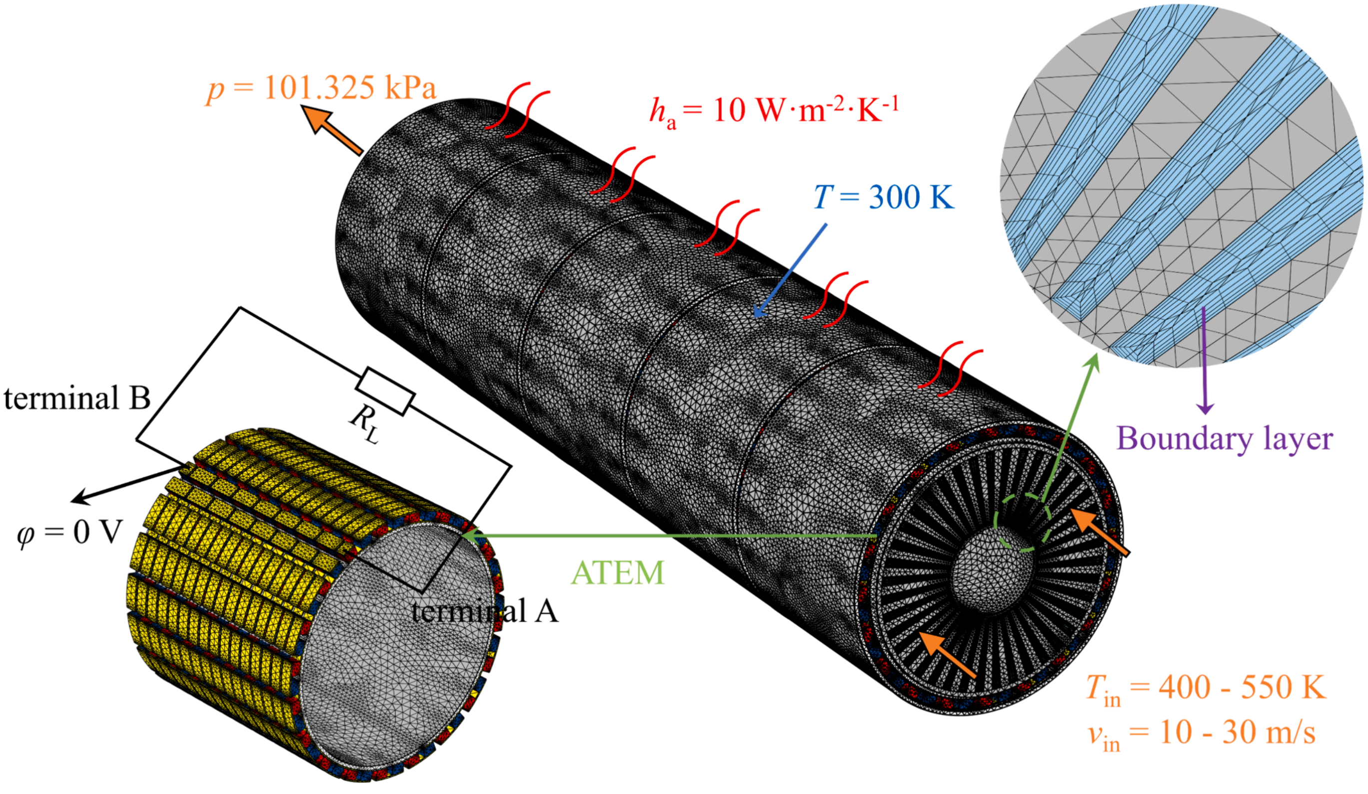

**Fig. 3.** Finite element model of the ATEG.

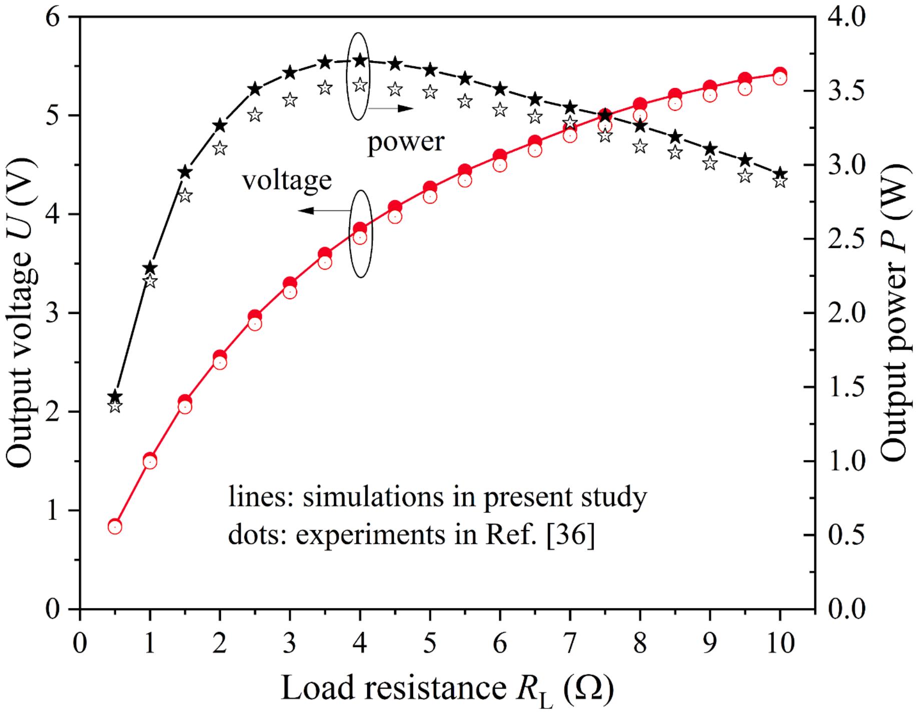

**Fig. 4.** Comparison between experiments in Ref. [36] and simulations in the present study.

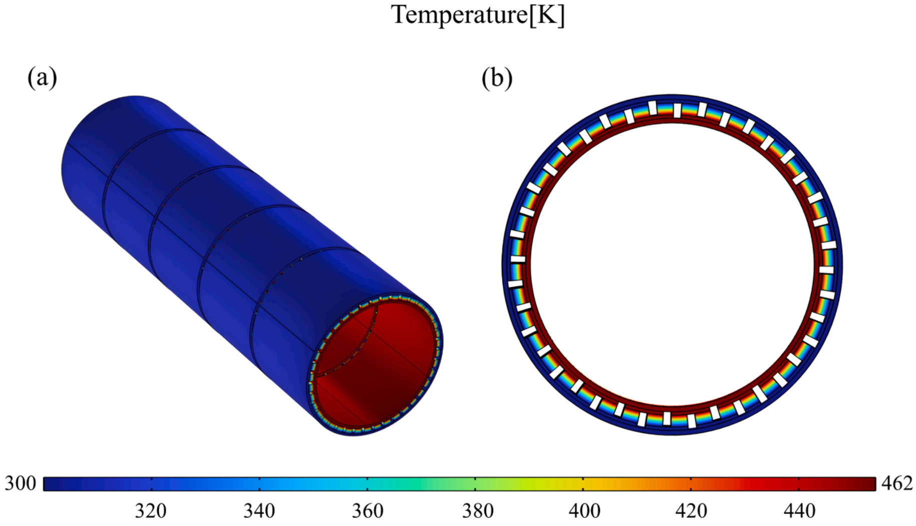

**Fig. 5.** Temperature distributions of the ATEM. (a) 3D view; (b) 2D view.

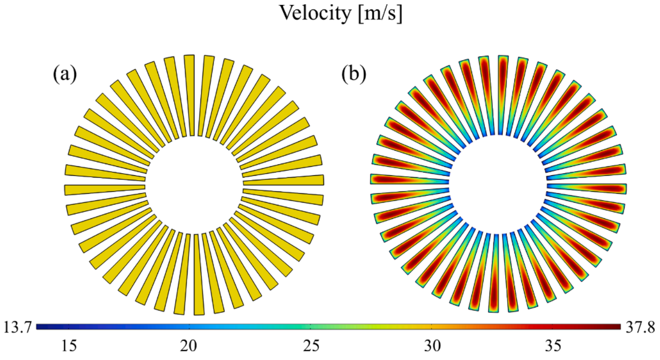

**Fig. 6.** Velocity distributions of the exhaust gas. (a) Inlet; (b) Outlet.

elements, resulting in the generation of electrical energy. Also, it is evident that the maximum hot-side temperature of 462 K is quite lower than the exhaust temperature (550 K), primarily due to the temperature drop from the exhaust gas to the heat exchanger. Consequently, the fin structure is adopted in the concentric annular heat exchanger to improve the hot-side temperature.

Fig. 6 shows the velocity distributions of the exhaust gas on the inlet and outlet surfaces. Although the application of a velocity inlet boundary condition on the inlet surface, as the exhaust gas flows downwards, it will concentrate at the center of the flow channel, leading to an increased flow velocity.

Fig. 7(a) depicts the temperature distributions of the exhaust gas. A notable temperature gradient is evident, extending from the exhaust inlet surface (550 K) to the exhaust outlet surface (377 K). The operational temperature of the ATEM's hot side is determined by the exhaust

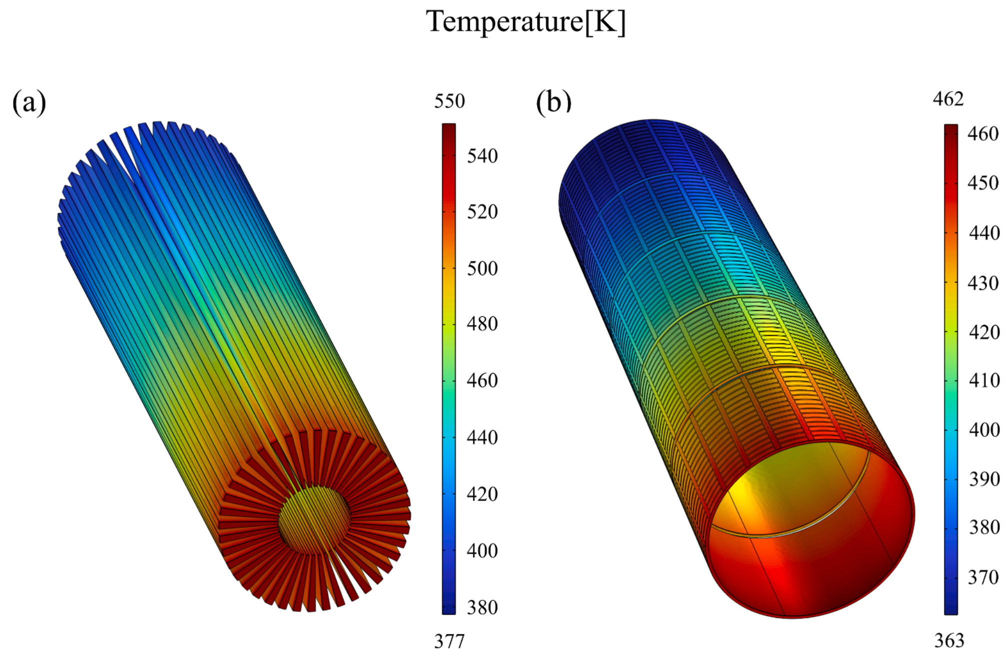

**Fig. 7.** Temperature distributions. (a) Exhaust gas; (b) Hot side of thermoelectric elements.

temperature of the corresponding region. Therefore, there is also a substantial decrease in the hot-side temperature of ATEMs, as shown in Fig. 7(b). The maximum temperature drop from the 1st ATEM to the 5th ATEM reaches 99 K, and the temperature drop in one single ATEM is about 20 K. The difference in the hot-side temperature of thermoelectric elements leads to uneven current distribution. However, in each ATEM, the connection of all thermoelectric elements is in series, and the uneven current inevitably leads to electrical energy loss. Therefore, the novel ATEM is proposed in this work to address this defect, where the cross-sectional area of thermoelectric elements continuously increases from the first column to the last column in each ATEM. This novel design, by increasing the cross-sectional area of thermoelectric elements in the downward direction, will generate a more uniform current across all thermoelectric elements, thereby enhancing the overall current of the ATEM. In addition, the maximum hot-side working temperature of the ATEM is only 462 K, which is lower than the allowable temperature for $Bi_2Te_3$-based thermoelectric materials. Therefore, the proposed ATEG can be applied to waste heat recovery with higher temperatures, such as the exhaust of natural gas-powered vehicles. In this condition, the ATEG can deliver greater output performance.

Fig. 8 shows the voltage distributions of the ATEG under $\Delta L = 0$ and $\Delta L = 0.06$ mm. As observed, the output voltage of the ATEM

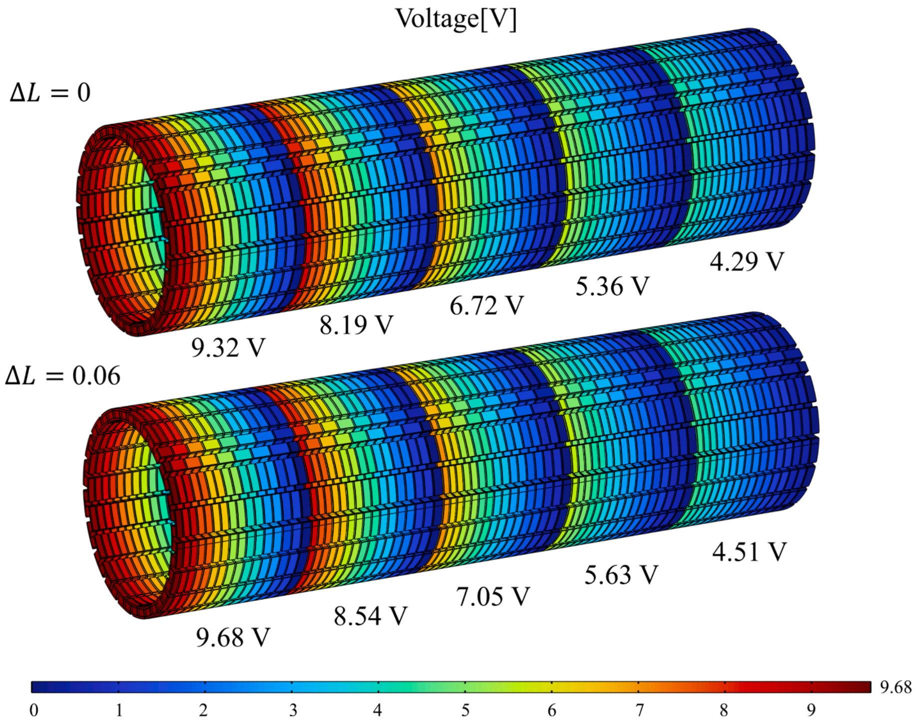

**Fig. 8.** Voltage distributions of the ATEG under $\Delta L = 0$ and $\Delta L = 0.06$ mm.

continuously diminishes from the first unit to the last unit due to the decrease in temperature resulting from the downward flow of exhaust gas. The output voltage of the last ATEM only accounts for approximately 46 % of the output voltage produced by the first column ATEM. The same phenomenon also exists between different columns in a single ATEM. For this reason, the novel ATEM structure is proposed to address this issue. As can be observed from the figure, the novel ATEM with ΔL = 0.06 mm outperforms the traditional structure (ΔL = 0), with the output voltage of the first and last ATEM increasing by 3.86 % and 5.13 %, respectively. However, the ΔL value requires further optimization, and a comprehensive analysis of the impact of diverse operating conditions on the optimum value is necessary.

### 4.2. Exploration of the optimal ΔL value

To explore the optimal ΔL value, ATEG models with different ΔL values are established and their output performance is comprehensively compared. It is worth noting that the ATEGs used for comparison all adopt the same amount of thermoelectric materials. For example, the ATEG uses five ATEMs with each including 16 columns of thermoelectric elements, and the total volume of thermoelectric elements in each ATEM is 35639.0 mm$^3$; In a traditional ATEM, the length of thermoelectric elements is fixed at L = 2 mm, while in the novel ATEM with ΔL = 0.06mm, the length of thermoelectric elements from the first column to the last column is $L_1$ = 1.55 mm, $L_2$ = 1.61 mm, …, and $L_{16}$ = 2.45 mm, respectively. Fig. 9 shows the output power of ATEMs with different ΔL values. When ΔL = 0.02 mm, 0.04 mm, and 0.06 mm, the output power of the novel ATEM in each unit is higher than that of the traditional ATEM. However, when ΔL = 0.08 mm, the output power of the traditional ATEM in each unit is higher than that of the novel ATEM. The reason for this phenomenon is that when ΔL = 0.08 mm, the increased cross-sectional area of the thermoelectric element along the downward direction is too large, which actually causes the current of the $i+1$th column of thermoelectric elements to be greater than the current of the ith column of thermoelectric elements. It appears that the optimal value for ΔL is 0.06 mm. By summing the output power of 5 ATEMs, it is found that the output power of the novel ATEG with ΔL = 0.06 mm reaches 76.66 W, which is 8.97 % higher than that of the traditional ATEG. However, the optimal ΔL value may alter with the variation of exhaust inlet boundary conditions. The impact of exhaust gas temperature and velocity on the performance of the novel ATEG is analyzed in the following sections.

### 4.3. Effect of exhaust gas temperature

Fig. 10(a) illustrates the output power of the ATEG in relation to exhaust gas temperature, considering different ΔL values. Here, the exhaust gas velocity is fixed at 30 m/s. On the one hand, it is clear that as the exhaust gas temperature increases, the output power of the ATEG continues to increase. On the other hand, regardless of temperature changes, when ΔL = 0.02 mm, 0.04 mm, and 0.06 mm, the output power of the novel ATEG is always higher than that of the traditional ATEG (ΔL = 0), especially when ΔL = 0.06 mm. As the increase of exhaust gas temperature from 400 K to 550 K, the output power of the optimal ATEG (ΔL = 0.06 mm) increases from 12.26 W to 76.66 W, while the power of the traditional ATEG increases from 9.56 W to 70.35 W. Meanwhile, compared to the traditional structure, the power improvement of the novel ATEG decreases from 28.24 % to 8.97 %. It seems that the advantages of the novel ATEG become more prominent at lower exhaust gas temperatures.

Fig. 10(b) shows the output efficiency of the ATEG with different ΔL values as a function of exhaust gas temperature. Similar to the output power, the variation trend in the output efficiency of the ATEG shows a close resemblance. This is because the change in the ATEM structure has little impact on the heat absorption $Q_h$ of the entire ATEG, and the efficiency is directly proportional to the power. The output efficiency of the optimal ATEG at the exhaust gas temperatures of 400 K, 450 K, 500 K, and 550 K is 0.56 %, 0.90 %, 1.11 %, and 1.45 %, respectively. Here,

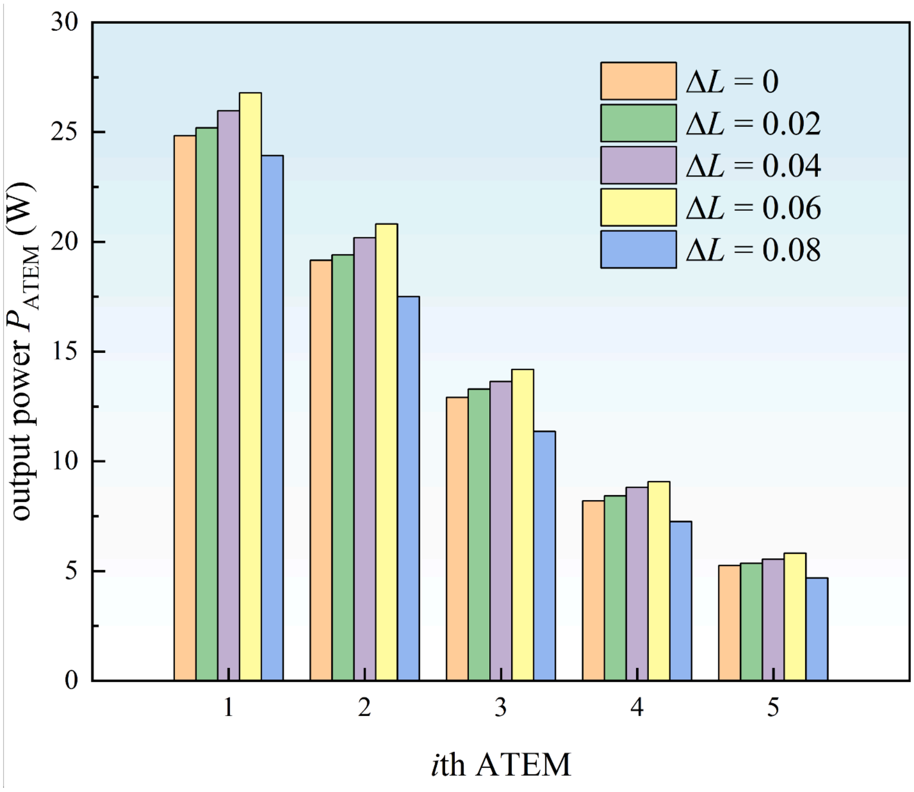

**Fig. 9.** Output power of the *i*th ATEM with different ΔL values.

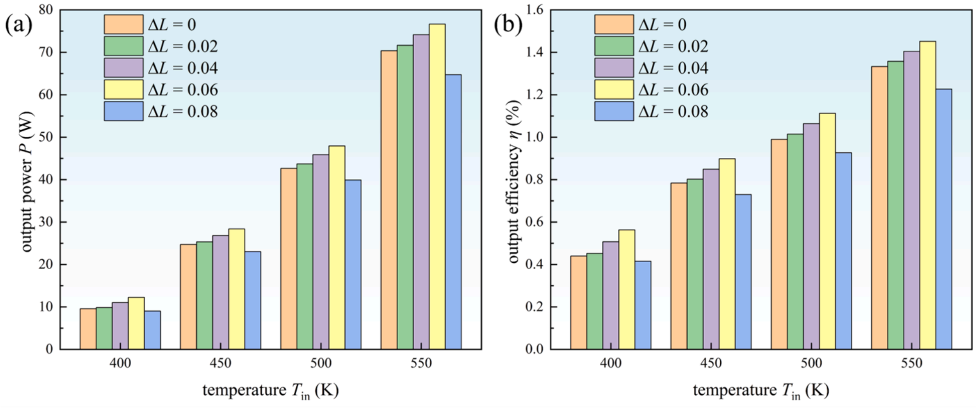

**Fig. 10.** Output performance of the ATEG with different ΔL values as a function of exhaust gas temperature. (a) Output power; (b) Output efficiency.

compared to the reported conversion efficiency of ~ 2 % in the literature [43], the relatively lower efficiency in the proposed ATEG is mainly caused by the low hot-side temperature of the ATEM (see Fig. 7(b)). When applied to situations with higher temperatures, the ATEG has the ability to reach higher conversion efficiency, even far exceeding 2 %. Compared with traditional ATEG with conversion efficiencies of 0.44 %, 0.78 %, 0.99 %, and 1.33 % at 400 K, 450 K, 500 K, and 550 K, the efficiency of the optimal ATEG is improved by 28.08 %, 14.60 %, 12.39 %, and 8.92 %, respectively. It can be concluded that the utilization of the proposed novel design results in a substantial enhancement in both the output power and output efficiency of the ATEG.

### 4.4. *Effect of exhaust gas velocity*

Fig. 11(a) illustrates the output power of the ATEG in relation to exhaust gas velocity, taking into account different ΔL values. Here, the exhaust gas temperature is fixed at 550 K. It can be seen that an increase in exhaust gas velocity helps to improve the output power of ATEG, as higher exhaust gas velocity results in a more vigorous heat transfer between the heat exchanger and the exhaust gas. Similarly, when ΔL = 0.06 mm, the output power of the novel ATEG reaches the highest value, while the ΔL value of 0.08 mm may deteriorate the output performance of the ATEG. At the exhaust gas velocity of 15 m/s, 20 m/s, 25 m/s, and 30 m/s, compared with the output power of 27 W, 43.22 W, 56.58 W, and 70.35 W for the traditional ATEG, the output power of the optimized ATEG reaches 30.88 W, 47.73 W, 62.11 W, and 76.66 W, experiencing an improvement of 14.37 %, 10.43 %, 9.77 %, and 8.97 %, respectively. The smaller the exhaust gas velocity, the greater the power improvement. This is because as the velocity increases, more exhaust gas participates in the gas-to-exchanger heat transfer, and the temperature drop along the downward direction of the exhaust gas diminishes, leading to a decreased efficacy of the proposed novel design.

The variation of output efficiency with exhaust gas velocity for ATEGs with different ΔL values is shown in Fig. 11(b), and the observed trend aligns consistently with that of the output power. As the exhaust gas velocity increases from 15 m/s to 30 m/s, the output efficiency of the traditional ATEG increases from 0.38 % to 1.33 %, while that of the optimized ATEG increases from 0.43 % to 1.45 %, with the efficiency improvement being a decrease from 14.25 % to 8.93 %. Combined with Fig. 10, it is concluded that with the increase of exhaust gas temperature and velocity, both output power and output efficiency of the ATEG significantly increase, however, the performance improvement caused by the novel ATEG decreases. Under the exhaust gas temperature of 550 K and the exhaust gas velocity of 30 m/s, the novel ATEG achieves an output power of 76.66 W and an output efficiency of 1.45 %. These values represent an improvement of 8.97 % and 8.93 %, respectively, compared to the traditional structure.

## 5. Conclusions

Within the domain of waste heat recovery, to address the issue of performance deterioration of the ATEG caused by the temperature drop, a novel ATEG structural design is proposed in this work, where the cross-sectional area of thermoelectric elements in each ATEM continuously

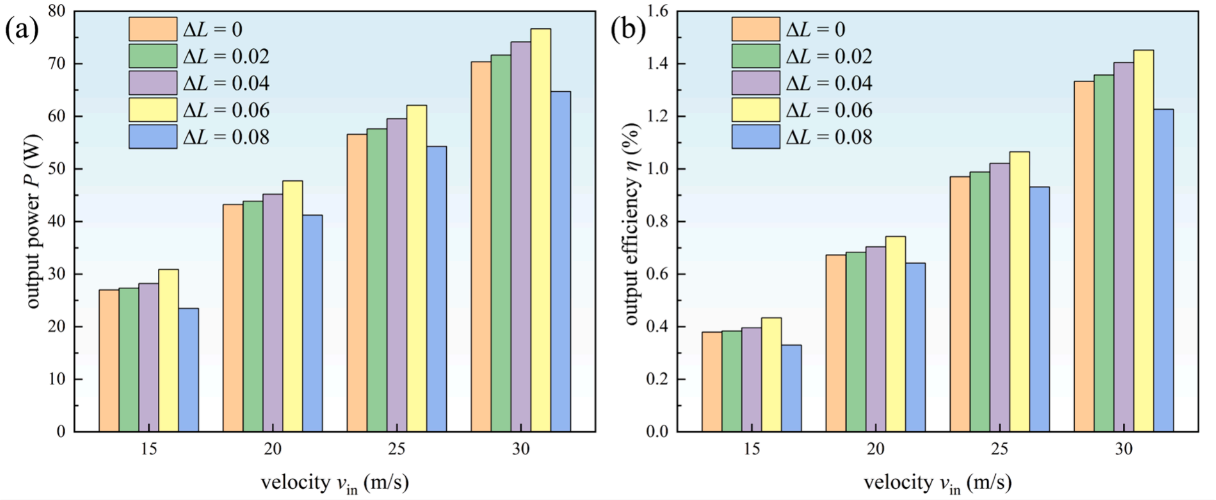

**Fig. 11.** Output performance of the ATEG with different ΔL values as a function of exhaust gas velocity. (a) Output power; (b) Output efficiency.

increases along the direction of exhaust gas flow. Besides, a fluid-thermal-electric multiphysics numerical model for the ATEG is established to assess its performance and perform parameter optimizations, with the length difference between adjacent columns of thermoelectric elements, ΔL, being comprehensively optimized. Also, the effect of exhaust gas temperature and velocity on the ΔL value is comprehensively analyzed. The findings are summarized as follows:

(1) The developed fluid-thermal-electric multiphysics numerical model is well verified using experimental data from previous studies. The model can accurately obtain the interior distribution characteristics of the ATEG at different working conditions, such as the temperature, velocity, and voltage distributions. Numerical results indicate that there is a significant temperature drop inside the ATEM along the downward direction of exhaust gas, highlighting the advantages and effectiveness of the proposed new configuration for thermoelectric modules.

(2) As the increase of ΔL value, the output power of the ATEG increases first and then decreases. When ΔL = 0.06 mm, the novel ATEG reaches the highest output performance. However, if the ΔL value is further increased, the oversized cross-sectional area of thermoelectric elements in the downward direction of exhaust gas will deteriorate the output performance of the ATEG. In addition, the optimal ΔL value is not sensitive to the exhaust gas temperature and velocity, which means that even if applied to waste heat recovery in different vehicles, the ΔL value of 0.06 mm is still optimal.

(3) Under the exhaust gas temperature of 550 K and the exhaust gas velocity of 30 m/s, the novel ATEG achieves an output power of 76.66 W and an output efficiency of 1.45 %. These values represent an improvement of 8.97 % and 8.93 %, respectively, compared to the traditional structure. Besides, the lower the exhaust gas temperature and velocity are, the more significant the benefits generated by the novel ATEG. For instance, as the increase of exhaust gas temperature from 400 K to 550 K, the power improvement of the novel ATEG decreases from 28.24 % to 8.97 %.

(4) The current research does not take into account the connections between different ATEMs. Instead, it calculates the overall output of the ATEG by summing individual outputs of ATEMs, and the ATEG consists of only five ATEMs, which does not align with real-world scenarios. Hence, future research will involve the development of a more comprehensive ATEG featuring multiple ATEMs and an exploration of the effects of topological connections between them.

## CRediT authorship contribution statement

**Ding Luo:** Writing – review & editing, Writing – original draft, Supervision, Methodology, Conceptualization. **Haokang Zhang:** Writing – original draft, Visualization, Validation, Investigation. **Jin Cao:** Data curation. **Yuying Yan:** Formal analysis. **Bingyang Cao:** Writing – review & editing, Supervision, Project administration, Funding acquisition.

## Declaration of competing interest

The authors declare that they have no known competing financial interests or personal relationships that could have appeared to influence the work reported in this paper.

## Data availability

Data will be made available on request.

## Acknowledgements

This work was supported by the National Natural Science Foundation of China (Nos. 52250273, U20A20301), the National Natural Science Foundation of China (52306017), and the Natural Science Foundation of Hubei Province (No. 2023AFB093).

## References

[1] Massaguer A, Massaguer E, Comamala M, Pujol T, Montoro L, Cardenas MD, et al. Transient behavior under a normalized driving cycle of an automotive thermoelectric generator. Appl Energy 2017;206:1282–96.

[2] Zhu W, Weng Z, Li Y, Zhang L, Zhao B, Xie C, et al. Theoretical analysis of shape factor on performance of annular thermoelectric generators under different thermal boundary conditions. Energy 2022;239:122285.

[3] Luo D, Yang S, Yan Y, Cao J, Cao B. Performance improvement of the automotive thermoelectric generator by extending the hot side area of the heat exchanger through heat pipes. Energy Convers Manage 2024;310:118472.

[4] Luo D, Yan Y, Chen W-H, Cao B. Exploring the dynamic characteristics of thermoelectric generator under fluctuations of exhaust heat. Int J Heat Mass Transfer 2024;222:125151.

[5] Yang W, Jin C, Zhu W, Xie C, Huang L, Li Y, et al. Innovative design for thermoelectric power generation: Two-stage thermoelectric generator with variable twist ratio twisted tapes optimizing maximum output. Appl Energy 2024;363:123047.

[6] Tian H, Chang L, Gao Y, Shu G, Zhao M, Yan N. Thermo-economic analysis of zeotropic mixtures based on siloxanes for engine waste heat recovery using a dual-loop organic Rankine cycle (DORC). Energ Conver Manage 2017;136:11–26.

[7] Zhang X, Wang X, Cai J, Wang R, Bian X, Wang J, et al. Selection maps of dual-pressure organic Rankine cycle configurations for engine waste heat recovery applications. Appl Therm Eng 2023;228:120478.

[8] Yang Z, Zhang Y, Dong Q, Lin J, Lin G, Chen J. Maximum power output and parametric choice criteria of a thermophotovoltaic cell driven by automobile exhaust. Renew Energy 2018;121:28–35.

[9] Javad DM. Enhancing energo-exergo-economic performance of Kalina cycle for low- to high-grade waste heat recovery: Design and optimization through deep learning methods. Appl Therm Eng 2021;195:117221.

[10] da Costa Horta GR, Barbosa EP, Moreira LF, Arrieta FRP, de Oliveira RN. Comparison of Kalina cycles for heat recovery application in cement industry. Appl Therm Eng 2021;195:117167.

[11] Gayner C, Kar KK. Recent advances in thermoelectric materials. Prog Mater Sci 2016;83:330–82.

[12] Pei J, Cai B, Zhuang H-L, Li J-F. $Bi_2Te_3$-based applied thermoelectric materials: research advances and new challenges. Natl Sci Rev 2020;7(12):1856–8.

[13] Luo D, Wang R, Yu W, Sun Z, Meng X. Modelling and simulation study of a converging thermoelectric generator for engine waste heat recovery. Appl Therm Eng 2019;153:837–47.

[14] Zhu W, Xu A, Yang W, Xiong B, Xie C, Li Y, et al. Optimal design of annular thermoelectric generator with twisted tape for performance enhancement. Energ Conver Manage 2022;270:116258.

[15] Yang W, Zhu W, Li Y, Zhang L, Zhao B, Xie C, et al. Annular thermoelectric generator performance optimization analysis based on concentric annular heat exchanger. Energy 2022;239:122127.

[16] Chen W-H, Chiou Y-B, Chein R-Y, Uan J-Y, Wang X-D. Power generation of thermoelectric generator with plate fins for recovering low-temperature waste heat. Appl Energy 2022;306:118012.

[17] Eldin SM, Alanazi M, Alanazi A, Alqahtani S, Alshehery S, Anqi AE. Economic and thermal analysis of a tubular thermoelectric power generator equipped with a novel fin-pin-porous based heat exchanger; comparative case study with conventional smooth channel. Case Stud Thermal Eng 2023;48:103166.

[18] Li Y, Wang S, Zhao Y, Yue L. Effect of thermoelectric modules with different characteristics on the performance of thermoelectric generators inserted in the central flow region with porous foam copper. Appl Energy 2022;327:120041.

[19] Yang W, Zhu W, Du B, Wang H, Xu L, Xie C, et al. Power generation of annular thermoelectric generator with silicone polymer thermal conductive oil applied in automotive waste heat recovery. Energy 2023;282:128400.

[20] Niu Z, Diao H, Yu S, Jiao K, Du Q, Shu G. Investigation and design optimization of exhaust-based thermoelectric generator system for internal combustion engine. Energ Conver Manage 2014;85:85–101.

[21] Wang R, Meng Z, Luo D, Yu W, Zhou W. A comprehensive study on X-type thermoelectric generator modules. J Electron Mater 2020;49:4343–54.

[22] Shen Z-G, Liu X, Chen S, Wu S-Y, Xiao L, Chen Z-X. Theoretical analysis on a segmented annular thermoelectric generator. Energy 2018;157:297–313.

[23] Lv H, Wang X-D, Meng J-H, Wang T-H, Yan W-M. Enhancement of maximum temperature drop across thermoelectric cooler through two-stage design and transient supercooling effect. Appl Energy 2016;175:285–92.

[24] Asaadi S, Khalilarya S, Jafarmadar S. A thermodynamic and exergoeconomic numerical study of two-stage annular thermoelectric generator. Appl Therm Eng 2019;156:371–81.

[25] Zhao Y, Li W, Zhao X, Wang Y, Luo D, Li Y, et al. Energy and exergy analysis of a thermoelectric generator system for automotive exhaust waste heat recovery. Appl Therm Eng 2024;239:122180.

[26] Hasan MN, Nayan N, Nafea M, Muthalif AGA, Mohamed Ali MS. Novel structural design of wearable thermoelectric generator with vertically oriented thermoelements. Energy 2022;259:125032.

[27] Araiz M, Casi Á, Catalán L, Martínez Á, Astrain D. Prospects of waste-heat recovery from a real industry using thermoelectric generators: economic and power output analysis. Energ Conver Manage 2020;205:112376.

[28] Shen Z-G, Wu S-Y, Xiao L. Assessment of the performance of annular thermoelectric couples under constant heat flux condition. Energ Conver Manage 2017;150:704–13.

[29] Buchalik R, Nowak G, Nowak I. Mathematical model of a thermoelectric system based on steady- and rapid-state measurements. Appl Energy 2021;293:116943.

[30] Huang B, Shen Z-G. Performance assessment of annular thermoelectric generators for automobile exhaust waste heat recovery. Energy 2022;246:123375.

[31] Jia Y, Zhang Z, Wang C, Sun H, Zhang W. Design and parameter study of a thermoelectric generator for waste heat recycling in flexible micro-light-emitting diodes. Appl Therm Eng 2022;200:117568.

[32] Lai C, Zhao Q, Zhang Z, Zhang H, Hou S, Zhao J. Potential evaluation of flexible annular thermoelectric generator in photovoltaic system performance improvement: Energy and exergy perspectives. Energ Conver Manage 2021;247:114711.

[33] Ge M, Wang X, Zhao Y, Wang S, Liu L. Performance analysis of vaporizer tube with thermoelectric generator applied to cold energy recovery of liquefied natural gas. Energ Conver Manage 2019;200:112112.

[34] Lu X, Yu X, Qu Z, Wang Q, Ma T. Experimental investigation on thermoelectric generator with non-uniform hot-side heat exchanger for waste heat recovery. Energ Conver Manage 2017;150:403–14.

[35] Luo D, Wang R, Yu W, Zhou W. Performance evaluation of a novel thermoelectric module with BiSbTeSe-based material. Appl Energy 2019;238:1299–311.

[36] Luo D, Wang R, Yu W, Zhou W. A novel optimization method for thermoelectric module used in waste heat recovery. Energ Conver Manage 2020;209:112645.

[37] Chen W-H, Liao C-Y, Hung C-I, Huang W-L. Experimental study on thermoelectric modules for power generation at various operating conditions. Energy 2012;45:874–81.

[38] Hu Q, Luo D, Guo J, Qiu W, Wu X, Yang L, et al. Broad Temperature plateau for high thermoelectric properties of n-Type Bi2Te2.7Se0.3 by 3D printing-driven defect engineering. ACS Appl Mater Interfaces 2022;15:1296–304.

[39] Luo D, Yan Y, Chen W-H, Yang X, Chen H, Cao B, et al. A comprehensive hybrid transient CFD-thermal resistance model for automobile thermoelectric generators. Int J Heat Mass Transf 2023;211:124203.

[40] Luo D, Wu Z, Yan Y, Cao J, Yang X, Zhao Y, et al. Performance investigation and design optimization of a battery thermal management system with thermoelectric coolers and phase change materials. J Clean Prod 2024;434:139834.

[41] Luo D, Zhao Y, Cao J, Chen W-H, Zhao Y, Cao B. Performance analysis of a novel thermoelectric-based battery thermal management system. Renew Energy 2024;224:120193.

[42] Luo D, Yan Y, Li Y, Yang X, Chen H. Exhaust channel optimization of the automobile thermoelectric generator to produce the highest net power. Energy 2023;281:128319.

[43] Pacheco N, Brito FP, Vieira R, Martins J, Barbosa H, Goncalves LM. Compact automotive thermoelectric generator with embedded heat pipes for thermal control. Energy 2020;197:117154.